Comparative Analysis of Photoluminescence and Upconversion Emission from Individual Carbon Nanotubes for Bioimaging Applications

Noémie Danné,[†,‡,⊥] Antoine G. Godin,[†,‡,⊥] Zhenghong Gao,[†,‡] Juan A. Varela,[§,∥] Laurent Groc,[§,∥] Brahim Lounis,[†,‡] and Laurent Cognet*[,†,‡]

[†]Université de Bordeaux, Laboratoire Photonique Numérique et Nanosciences, UMR 5298, F-33400 Talence, France

[‡]Institut d'Optique & CNRS, LP2N UMR 5298, F-33400 Talence, France

[§]Université de Bordeaux, Interdisciplinary Institute for Neuroscience, UMR 5297, F-33000 Bordeaux, France

[∥]CNRS, IINS UMR 5297, F-33000 Bordeaux, France

ABSTRACT: Luminescent single-walled carbon nanotubes (SWCNTs) are unique nanoemitters that allow near-infrared single-molecule detection within biological tissues. Interestingly, the recent discovery of upconversion luminescence from (6,5) SWCNTs provides a novel opportunity for deep tissue single SWCNT detection. Yet, the optimal excitation strategy for video-rate imaging of individual SWCNTs within live tissues needs to be determined taking into account the constraints imposed by the biological matter. Here, we directly compare the luminescence efficiencies of single (6,5) SWCNTs excited by continuous-wave lasers at their second-order excitonic transition, at their K-momentum exciton−phonon sideband, or through upconversion. For these three excitations spanning visible to near-infrared wavelengths, the relevance of single SWCNT imaging is considered inside brain tissue. The effects of tissue scattering, absorption, autofluorescence, and temperature increase induced by excitation light are systematically examined.

KEYWORDS: *single-walled carbon nanotube, photoluminescence, upconversion, single-molecule imaging, bioimaging*
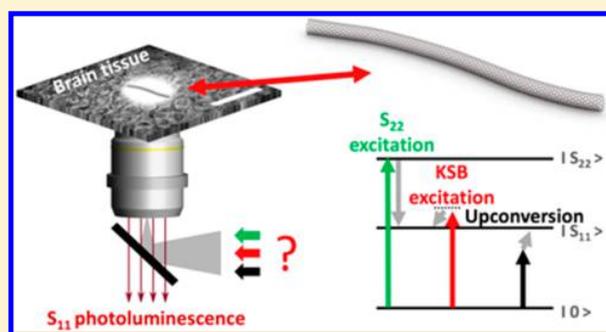
Over the past decade, single-molecule microscopy has emerged as the ultimate strategy for imaging and understanding biological phenomena in living cells. The detection of single nano-objects provides invaluable insights about their micro- to nanoscale environments and further allows super-resolution imaging.[1] Accessing such information in intact organs rather than isolated cells is more challenging and requires small-size nanoprobes displaying stable and bright optical signals in high absorption and scattering environments. To this aim, near-infrared (NIR) emission drastically improves light penetration and detection in tissues. Single-walled carbon nanotubes (SWCNTs) have recently been shown to be unrivaled single-molecule probes due to their excellent NIR photoluminescence (PL) properties and their unique 1D morphology for propagation in tissues.[1−4]

At the ensemble level, SWCNTs can be imaged in animals over long periods of time, demonstrating their low toxicity in live specimens.[5,6] Several wavelengths have been used to excite specific nanotube absorption bands that fall in the biological "transparency" window.[4,7,8] At the single-molecule level, the inherent low signals impose more constraints in the choice of chiralities with favorable emission and absorption properties to achieve high signal-to-noise ratios (SNRs) in tissues. Although several chiralities can be used,[9] (6,5) SWCNTs benefit from an

established ability to allow long-term single-nanotube tracking with negligible photobleaching in live cells[10] and live brain tissue.[4] Here we investigate the optimal excitation strategy for video-rate imaging luminescent (6,5) SWCNTs at the single-nanotube level in biological tissues with high SNRs. We consider nanotube absorption and PL properties together with tissue scattering and absorption, which inevitably lead to tissue autofluorescence and temperature increase depending on the excitation wavelength.

There are different options for efficient excitation of SWCNT luminescent species[11] at the single-tube level. While resonant excitation at the second-order excitonic transition, S_{22}, is commonly used, the K-momentum exciton−phonon sideband excitation, KSB, offers, in principle, better luminescence photo-stability[12] and tissue penetration. However, KSB excitation is less efficient and thus requires higher intensities to achieve identical nanotube PL brightness.[12] Recently, upconversion luminescence (UCL) has been demonstrated for excitation of (6,5) SWCNTs, using pulsed excitation with photon energies smaller that the S_{11} exciton recombination energy[13,14] (see Figure 1A). Although the mechanism underlying upconversion
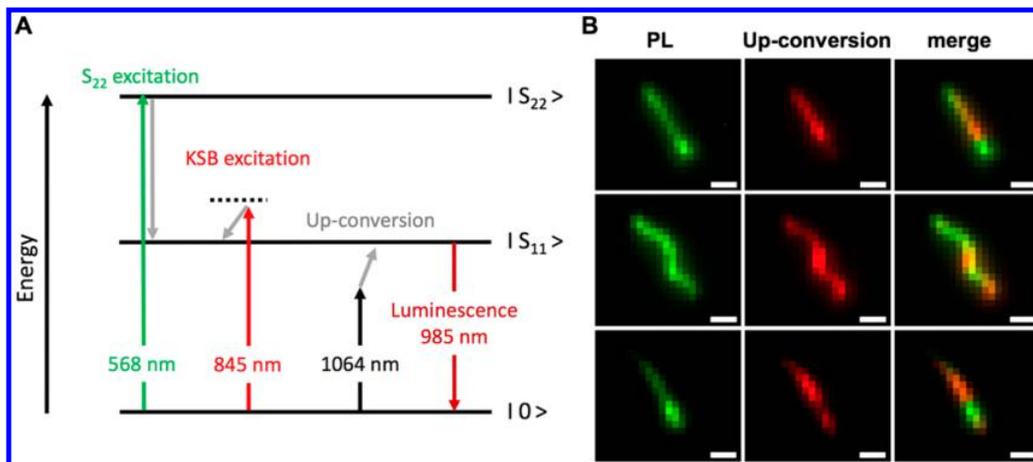
Figure 1. (A) Diagram showing the different excitation strategies for obtaining luminescent (6,5) SWCNTs. (B) Luminescence images of micrometer long (6,5) nanotubes suspended in NaDOC, using 568 nm photoexcitation (0.2 kW/cm²) or 1064 nm upconversion (3.2 kW/cm²) with cw lasers in a wide-field configuration. Spatially anticorrelated luminescence signals are frequently observed between the two excitation schemes. Integration time: 100 ms. Scale bar = 1 μm.

excitation of the first-order excitonic transition is not fully understood in SWCNTs, this observation fostered great hopes for applications in bioimaging owing to its red-shifted excitation.

RESULTS AND DISCUSSION

We first imaged micrometer-long (6,5) luminescent SWCNTs suspended in sodium deoxycholate (NaDOC) excited at their S_{22} resonance (568 nm, see Methods). We selected those displaying bright albeit nonuniform PL along their backbone (Figure 1B). With NaDOC being one of the best encapsulation agents for obtaining bright (6,5) luminescent SWCNTs,[15−17] low-emitting regions of these SWCNTs must be due to the presence of quenching defects[18−20] such as structural defects induced by sonication during the encapsulation process (see Methods). When excited by a continuous-wave (cw) 1064 nm laser beam, UCL is efficiently induced at comparable average intensities compared with previous UCL reports using pulsed excitation[13,14] and thus does not require the high peak intensities of pulsed excitations. Strikingly, Figure 1B shows that UCL is generally the brightest in low-emitting PL regions, indicating that in SWCNTs UCL is favored by the presence of defect states. This observation suggests that UCL in SWCNTs involves low-lying energy defect states as proposed by Akuziki et al.[13]

For applications in bioimaging, NaDOC nanotubes are not biocompatible and therefore cannot be used. Recently, phospholipid-polyethylene glycol (pl-PEG) nanotubes were identified as the preferable choice for single-nanotube imaging experiments in live biological samples.[21] In the following, we thus investigate luminescent SWCNTs suspended by pl-PEG for imaging applications in biological tissues.[5,22,23] Figure 2A shows typical images of the same individual (6,5) pl-PEG-coated SWCNTs spin-coated on a microscope glass coverslip and excited in a wide-field configuration at 568 nm for resonant S_{22} excitation, 845 nm for resonant KSB excitation, or 1064 nm for UCL (see Figure 1A and Methods section). All beams were circularly polarized to ensure that SWCNTs are equally excited regardless of their orientation in the sample plane. Figure 2A shows that efficient UCL from pl-PEG-coated SWCNTs can also be observed. Moreover, the signal photostability is excellent (more than 6 min continuous recording in Figure 2B).
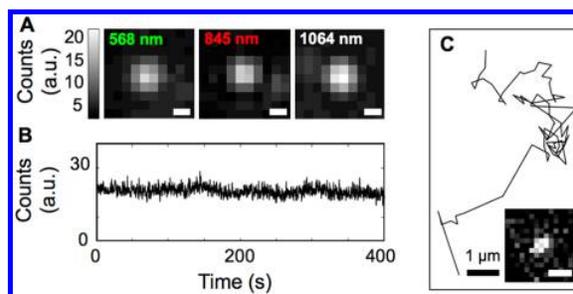

Figure 2. pl-PEG-suspended (6,5) SWCNTs. (A) Luminescence images of a single (6,5) excited SWCNT using either 568, 845, or 1064 nm cw lasers in a wide-field configuration (from left to right, respectively). Laser intensity: 0.4 kW/cm² (568 nm), 1.6 kW/cm² (845 nm), and 6.4 kW/cm² (1064 nm). Integration time: 100 ms. Scale bar = 500 nm. (B) UCL signal of a single (6,5) PLPEG-SWCNT recorded over 400 s. Laser intensity: 6.4 kW/cm², 100 ms integration time per point. (C) Single-nanotube tracking showing the 2D trajectory of a single (6,5) SWCNT diffusing in biological medium (DMEM) imaged by UCL using a 1064 nm cw laser (30 ms per frame). Laser intensity: 3.2 kW/cm².

Consequently, we performed single-particle tracking of SWCNTs detected by UCL in liquid environments. Figure 2C indeed demonstrates that single tubes diffusing in biological medium (DMEM, Dulbecco's modified Eagle medium) can be imaged efficiently at video rate and that their trajectories can be reconstructed.

In order to compare the luminescence efficiency under the different excitation mechanisms, we studied the average detected count rates per pixel from individual (6,5) SWCNTs encapsulated by pl-PEG as a function of laser intensity for the three different wavelengths (see Figure 3A). As expected, excitation at the S_{22} transition is the most efficient. Both S_{22} and KSB excitations display linear behaviors at low excitation intensities. In addition and accordingly to previous studies performed under pulsed excitation,[13] UCL displays a slightly sublinear intensity dependence with cw 1064 nm excitation. This rules out any multiphoton process that could excite the band-edge exciton.[13] A comparative analysis of the luminescence efficiency—defined as the slopes of the linear dependencies
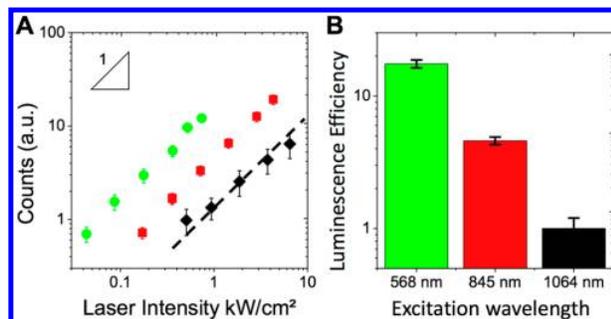
Figure 3. (A) Average luminescence signals from single (6,5) SWCNTs as a function of cw laser excitation intensities at 568, 845, or 1064 nm. N = 16, 13, and 12 SWCNTs respectively for each wavelength (green for 568 nm, red for 845 nm, and black for 1064 nm excitations). UCL data are approximated by a linear function (dotted line). (B) Comparison of SWCNT luminescence efficiencies, which represent the slopes of the linear dependence in luminescence signals measured in (A) for the three wavelengths. The relative efficiencies of 17.5 ± 1.2, 4.6 ± 0.3, and 1.0 ± 0.2 (for 568, 845, and 1064 nm, respectively) were normalized by the value obtained at 1064 nm.

shown in Figure 3A—for the three excitation wavelengths can then be performed (for this we consider a linear intensity dependence of UCL, as indicated by the dotted line in Figure 3A): S_{22} excitation is up to 4 times more efficient than KSB excitation in accordance with ensemble absorption spectra[24] and more than 1 order of magnitude more efficient than upconversion at 1064 nm (Figure 3B).

These results bring the question of the optimal excitation strategy for performing the detection of single (6,5) SCWNTs deep in biological samples while ensuring live tissue integrity. Indeed, imaging in live biological environments imposes that several additional factors apart from nanotube brightness must be considered, namely, tissue scattering and absorption, which lead to autofluorescence and temperature elevations. In the present case, while the reddest excitation light at 1064 nm ensures minimal tissue scattering and blood absorption, it cannot excite nanotubes as efficiently as the two other excitation wavelengths. Moreover, 1064 nm light is more absorbed by water than the two other wavelengths. Below, we quantify these different factors for realistic application of single (6,5) nanotube imaging in live tissues.

During light propagation in tissues, the amount of scattered light per unit length (μ_s) can be modeled as a function of wavelength by[25]

$$\mu_s(\lambda) = a \cdot \left(f_{Rayl} \left(\frac{\lambda}{500(nm)} \right)^{-4} + (1 - f_{Rayl}) \left(\frac{\lambda}{500(nm)} \right)^{-b_{Mie}} \right)$$

where a is a scaling factor and the first term corresponds to Rayleigh scattering, while the second to Mie scattering (b_{Mie} is the so-called Mie scattering power) with relative importance f_{Rayl} and $(1 - f_{Rayl})$, respectively. All these terms depend on the studied biological media. Here we consider the case of brain tissues consisting primarily of water, blood (hemoglobin, HGb), and fat[25] (see Table 1). In addition to scattering, tissue light absorption must be taken into account by writing the energy absorbed per unit of length (μ_a):[25]

$$\mu_a(\lambda) = BS\mu_{a,oxy}(\lambda) + B(1 - S)\mu_{a,deoxy}(\lambda) + W\mu_{a,water}(\lambda)$$
$$+ F\mu_{a,fat}(\lambda)$$

Table 1. Scattering and Absorption Contributions in Rat Brain Cortex

λ (nm)	$\mu_{a,oxy}$ (cm^{-1})	$\mu_{a,deoxy}$ (cm^{-1})	$\mu_{a,water}$ (cm^{-1})	$\mu_{a,fat}$ (cm^{-1})	μ_a (cm^{-1})	μ_s total (cm^{-1})
568	300	300	6.5×10^{-4}	6.5×10^{-2}	9	21.5
845	5	3	5×10^{-2}	6.5×10^{-2}	0.17	11.7
1064	3	0.5	8×10^{-1}	4×10^{-1}	0.7	8.7

The terms $\mu_{a,oxy}$ and $\mu_{a,deoxy}$ represent absorption by oxygenated and deoxygenated HGb, $\mu_{a,water}$ absorption by water, and $\mu_{a,fat}$ absorption by lipids with respective values that can be found in ref 25 (Table 1). B is the average blood volume fraction (3%), S is the HGb oxygen saturation of mixed arteriovenous vasculature (60%),[25] W is the fraction of water (77%),[26] and F is the fraction of fat (~10%).[27] Other constituents of the brain, such as inorganic salt and proteins, which represent ~10% of its content, have negligible contributions to the brain optical absorption in the visible and NIR. We can then calculate the amount of light absorption and scattering per unit of length at the three wavelengths mentioned above (Table 1). As expected, scattering is monotonically reduced with increasing wavelength, while absorption is minimal at 845 nm due to opposite evolutions of HGb and water absorptions (and fat to a lesser extent).

Tissue autofluorescence must also be taken into account as a process restricting nanotube SNRs. Although a small amount of quantitative data is available concerning tissue autofluorescence in the emission band of (6,5) SWCNTs, a general trend points toward a decreasing contribution for the reddest excitations.[28] Yet, the impact of tissue absorption, scattering, and autofluorescence on the SNR at which single luminescent (6,5) SWCNTs can be realistically detected in a tissue remains to be investigated.

For this, pl-PEG-coated SWCNTs were injected in the lateral cerebroventricles of rat brains. This brain injection method minimizes tissue inflammation and preserves the most native structure and integrity of brain tissues[29] while SWCNTs diffuse within distinct brain areas.[4] After 30 min, animals were sacrificed and ~100 μm thick brain slices were prepared for observation. The slices were fixed and stained with 4′,6-diamidino-2-phenylindole (DAPI) for identification of cell nuclei (see Methods and Figure 4A,B). In these fixed slices, single (6,5) SWCNTs were detected away from cell nuclei in the extracellular space (~50 μm deep inside the slice significantly further away from the surface slice surface to avoid the damaged superficial layers, Figure 4C−E). Excitation intensities of the three wavelengths were adjusted to collect, on average, identical PL count rates from individual SWCNTs. As expected, mean signal-to-background ratios are clearly improved for 1064 nm and to a lesser extent for 845 nm as compared to 568 nm: we find ~2.5, 0.3, and <0.1, respectively. This is because the weakest photoluminescence background is obtained at 1064 nm excitation, although the illumination intensity was the highest. Yet, for single-molecule detection, the SNR is the key parameter to be considered. In this context, 1064 and 845 nm excitations provide nearly identical performances (SNR ≈ 25), much better than at 568 nm (SNR < 5).

We finally quantified the impact of light absorption on tissue integrity by calculating the profile of temperature rise induced by light absorption. We used the COMSOL Multiphysics software to solve the heat equation for the three excitation wavelengths. The stationary heat equation is written

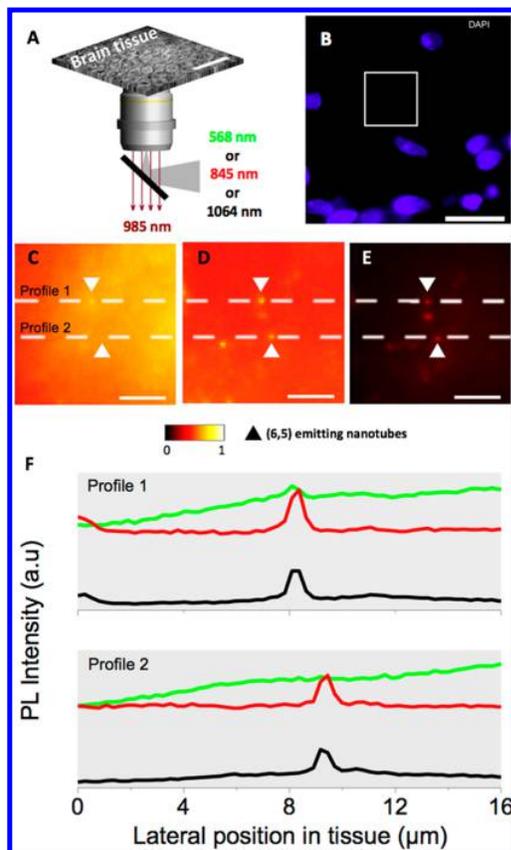$$-\mathrm{div}(k \overrightarrow{\mathrm{grad}}(T)) = I_{abs}(r, z)$$

Figure 4. (A) Schematics of the experimental setup used to image single (6,5) SWCNTs in a brain slice. (B) DAPI staining of the brain slice was used to identify cell nuclei. The highlighted square depicts the region shown in (C)−(E), where single SWCNTs are imaged. Scale bar = 20 μm. (C−E) Single (6,5) SWCNTs imaged 50 μm inside a brain slice (arrows) using laser excitations at 568 nm (C), 845 nm (D), or 1064 nm (E) in a wide-field configuration. Scale bar = 5 μm. The laser intensities were adjusted to obtain comparable SWCNT luminescence signals. (F) Signal obtained from the profiles indicated in (C)−(E) (green for 568 nm, red for 845 nm, and black for 1064 nm excitations).

with k being the thermal conductivity.

In our simulation presented in Figure 5, we considered a 1 cm^2 cylindrical tissue slice with a thickness of 2 mm immersed in water deposited on a 170 μm thick glass slide. A microscope objective, the temperature of which is set at 37 °C as a boundary condition, was positioned below the glass slide. The slice was illuminated along its symmetry axis by a 50 μm wide (fwhm) parallel Gaussian beam. To compensate for tissue absorbance, we considered laser intensities (0.23 kW/cm^2 for 568 nm, 0.80 kW/cm^2 for 845 nm, and 3.64 kW/cm^2 for 1064 nm) to induce equivalent luminescence rates for single nanotubes located 50 μm inside the tissue (Figure 3). The thermal conductivities of the brain tissue[30] (0.539 W/(m·K)) and silica (1.3 W/(m·K)) were considered temperature independent.

Figure 5 clearly shows that 1064 nm excitation raises the tissue temperature by up to 15 K, while the temperature increase is restricted to 8 and 0.8 K for 568 and 845 nm excitation, respectively. Obviously, 1064 nm illumination might be problematic for tissue integrity when using UCL for imaging individual SWCNTs in a live biospecimen, mainly because of
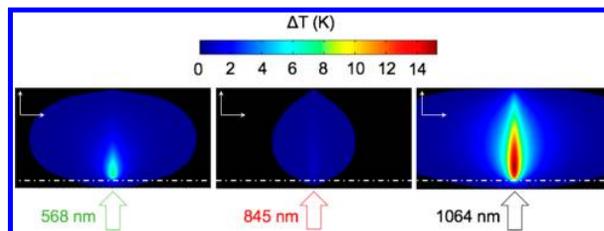

Figure 5. Simulation of heat elevation of brain tissue that was induced by laser excitation at 568, 845, or 1064 nm when laser excitation intensities are set to excite an individual (6,5) SWCNT situated 50 μm inside the tissue and displaying identical luminescence. The laser intensities are 0.23 kW/cm^2 for 568 nm excitation, 0.80 kW/cm^2 for 845 nm excitation, and 3.64 kW/cm^2 for 1064 nm excitation, which corresponds to respectively 0.20, 0.75, and 3.47 kW/cm^2 at the nanotube to correct for tissue absorbance. The dotted line indicates the interface between the coverslip and the tissue. Excitation beams are incident from the bottom as indicated by the arrows. Vertical and horizontal scale bars: 500 μm.

water absorption at this wavelength. In comparison, PL imaging using KSB 845 nm excitation leads to a modest increase of the tissue temperature.

In this work, we have demonstrated the video-rate imaging of single (6,5) SWCNTs diffusing in liquid environments upon cw UCL excitation at 1064 nm. We have compared the PL with UCL efficiencies of biocompatible pl-PEG-coated (6,5) SWCNTs. This allowed a realistic determination of the best excitation strategy to detect single (6,5) SWCNTs in live biological tissue. Unequivocally, by taking the example of brain tissue, we find that despite its most red-shifted wavelength, care should be taken when UCL aims at being used to image single SWCNTs at video rate in live tissues because of the temperature rise induced in the tissue. We showed that excitation at the K-momentum exciton−phonon sideband is the optimal strategy. A further fundamental understanding of the processes underlying UCL of SWCNTs might help in optimizing excitation efficiencies of single SWCNTs, by, for example, engineering chemical defects on the nanotube backbone.[31]

■ METHODS

SWCNT Preparation. HiPco-synthesized nanotubes (batch no. 195.7, Rice University) were suspended using NaDOC or pl-PEG molecules (#MPEG-DSPE-5000, Laysan Bio, Inc.). For NaDOC suspensions, SWCNTs were mixed in 1% w/v NaDOC in D$_2$O, and a brief tip sonication was applied (6 W output for 15 s) to obtain micrometer-long SWCNTs. For pl-PEG suspensions, 1 mg of raw SWCNTs and 5 mg of pl-PEG were added to 5 mL of D$_2$O and dispersed by tip sonication (20 W output for 8 min in an ice bath). D$_2$O was indeed found to provide more efficient dispersions than H$_2$O. SWCNT bundles and impurities were precipitated by ultracentrifugation (18000g for 60 min). The supernatant was then collected and stored at 4 °C. The concentration of pl-PEG SWCNT solution was estimated to 3 μg/mL. For spectroscopic experiments, a 10 μL drop of SWCNT suspension was spin-coated on glass coverslips. Brain injections were performed within 48 h after pl-PEG SWCNT suspension preparation.

Wide-Field Fluorescence Microscopy Setup. Single-SWCNT photoluminescence imaging was performed with an inverted microscope equipped with an electron multiplying CCD camera (Princeton Instruments ProEm) and a 1.40 NA 60× oil immersion objective in a wide-field configuration. Several excitation

sources were used to excite the (6,5) nanotubes: a 568 nm cw solid-state laser (Saphirre Coherent), a Ti:Sa laser tuned at 845 nm (Spectra Physics), and a 1064 nm cw Nd:YAG laser (Mephisto Coherent). All excitation beams were circularly polarized. A long-pass dichroic mirror (FF875-Di01, Semrock) was used for both S_{22} and KSB excitations, while for UCL a short-pass dichroic mirror was used instead (Edmund Opics dichroic short pass 1050 nm) to illuminate the samples. For all experiments, a combination of a long-pass emission filter (ET900LP, Chroma) and a short-pass filter (FESH 1000 Thorlabs) was used to specifically collect the photoluminescence of the (6,5) SWCNTs.

Intraventricular Injections and Slice Preparation. Sprague−Dawley rats (Janvier), treated according to the guidelines of the University of Bordeaux/CNRS Animal Care and Use Committee, were used for this work. Pl-PEG-coated SWCNTs were injected in the lateral cerebroventricles of young rat brain. Rats were sacrificed 30 min after the ventricular injection, and brain slices were then prepared for observation. The injections of SWCNTs were performed in 2-day-old living Sprague−Dawley rats anesthetized by hypothermia. Approximately 5 μL of the SWCNT dispersion was injected in each lateral ventricle at a depth of 2.9 mm. The injection site was found under cold light illumination by drawing a virtual line between the eye and lambda (seen through the skin), finding the midpoint of that line, and then moving 2 mm caudal from that midpoint along the virtual line. Brains were fixed with 4% paraformaldehyde for 4 h, washed in phosphate-buffered saline for 24 h, and subsequently sliced with a Vibratom into 100 μm thick slices. Fixed slices were then mounted on glass slides with Vectashield containing DAPI (Vector Laboratories).

■ AUTHOR INFORMATION

Corresponding Author
*E-mail: laurent.cognet@u-bordeaux.fr.

ORCID ◉
Laurent Cognet: 0000-0002-3573-5387

Author Contributions
[⊥]N. Danné and A. G. Godin contributed equally to this work.

Notes
The authors declare no competing financial interest.

■ REFERENCES

(1) Godin, A. G.; Lounis, B.; Cognet, L. Super-Resolution Microscopy Approaches for Live Cell Imaging. *Biophys. J.* **2014**, *107*, 1777−1784.

(2) Cherukuri, P.; Gannon, C. J.; Leeuw, T. K.; Schmidt, H. K.; Smalley, R. E.; Curley, S. A.; Weisman, R. B. Mammalian Pharmacokinetics of Carbon Nanotubes Using Intrinsic Near-Infrared Fluorescence. *Proc. Natl. Acad. Sci. U. S. A.* **2006**, *103*, 18882−18886.

(3) Wang, Y.; Bahng, J. H.; Che, Q.; Han, J.; Kotov, N. A. Anomalously Fast Diffusion of Targeted Carbon Nanotubes in Cellular Spheroids. *ACS Nano* **2015**, *9*, 8231−8238.

(4) Godin, A. G.; Varela, J. A.; Gao, Z.; Danné, N.; Dupuis, J. P.; Lounis, B.; Groc, L.; Cognet, L. Single-Nanotube Tracking Reveals the Nanoscale Organization of the Extracellular Space in the Live Brain. *Nat. Nanotechnol.* **2017**, *12*, 238−243.

(5) Welsher, K.; Liu, Z.; Sherlock, S. P.; Robinson, J. T.; Chen, Z.; Daranciang, D.; Dai, H. A Route to Brightly Fluorescent Carbon Nanotubes for Near-Infrared Imaging in Mice. *Nat. Nanotechnol.* **2009**, *4*, 773−780.

(6) Iverson, N. M.; Barone, P. W.; Shandell, M.; Trudel, L. J.; Sen, S.; Sen, F.; Ivanov, V.; Atolia, E.; Farias, E.; McNicholas, T. P.; Reuel, N.; Parry, N. M. A.; Wogan, G. N.; Strano, M. S. In Vivo Biosensing via Tissue-Localizable Near-Infrared-Fluorescent Single-Walled Carbon Nanotubes. *Nat. Nanotechnol.* **2013**, *8*, 873−880.

(7) Cherukuri, P.; Bachilo, S. M.; Litovsky, S. H.; Weisman, R. B. Near-Infrared Fluorescence Microscopy of Single-Walled Carbon Nanotubes in Phagocytic Cells. *J. Am. Chem. Soc.* **2004**, *126*, 15638−15639.

(8) Diao, S.; Hong, G.; Antaris, A. L.; Blackburn, J. L.; Cheng, K.; Cheng, Z.; Dai, H. Biological Imaging Without Autofluorescence in the Second Near-Infrared Region. *Nano Res.* **2015**, *8*, 3027−3034.

(9) Roxbury, D.; Jena, P. V.; Williams, R. M.; Enyedi, B.; Niethammer, P.; Marcet, S.; Verhaegen, M.; Blais-Ouellette, S.; Heller, D. A. Hyperspectral Microscopy of Near-Infrared Fluorescence Enables 17-Chirality Carbon Nanotube Imaging. *Sci. Rep.* **2015**, *5*, 14167.

(10) Fakhri, N.; Wessel, A. D.; Willms, C.; Pasquali, M.; Klopfenstein, D. R.; MacKintosh, F. C.; Schmidt, C. F. High-Resolution Mapping of Intracellular Fluctuations Using Carbon Nanotubes. *Science* **2014**, *344*, 1031−1035.

(11) Bachilo, S. M.; Strano, M. S.; Kittrell, C.; Hauge, R. H.; Smalley, R. E.; Weisman, R. B. Structure-Assigned Optical Spectra of Single-Walled Carbon Nanotubes. *Science* **2002**, *298*, 2361−2366.

(12) Santos, S. M.; Yuma, B.; Berciaud, S.; Shaver, J.; Gallart, M.; Gilliot, P.; Cognet, L.; Lounis, B. All-Optical Trion Generation in Single-Walled Carbon Nanotubes. *Phys. Rev. Lett.* **2011**, *107*, 187401.

(13) Akizuki, N.; Aota, S.; Mouri, S.; Matsuda, K.; Miyauchi, Y. Efficient Near-Infrared Up-Conversion Photoluminescence in Carbon Nanotubes. *Nat. Commun.* **2015**, *6*, 8920.

(14) Aota, S.; Akizuki, N.; Mouri, S.; Matsuda, K.; Miyauchi, Y. Upconversion Photoluminescence Imaging and Spectroscopy of Individual Single-Walled Carbon Nanotubes. *Appl. Phys. Express* **2016**, *9*, 045103.

(15) Wenseleers, W.; Vlasov, I. I.; Goovaerts, E.; Obraztsova, E. D.; Lobach, A. S.; Bouwen, A. Efficient Isolation and Solubilization of Pristine Single-Walled Nanotubes in Bile Salt Micelles. *Adv. Funct. Mater.* **2004**, *14*, 1105−1112.

(16) Haggenmueller, R.; Rahatekar, S. S.; Fagan, J. A.; Chun, J.; Becker, M. L.; Naik, R. R.; Krauss, T.; Carlson, L.; Kadla, J. F.; Trulove, P. C.; Fox, D. F.; DeLong, H. C.; Fang, Z.; Kelley, S. O.; Gilman, J. W. Comparison of the Quality of Aqueous Dispersions of Single Wall Carbon Nanotubes Using Surfactants and Biomolecules. *Langmuir* **2008**, *24*, 5070−5078.

(17) Duque, J. G.; Pasquali, M.; Cognet, L.; Lounis, B. Environmental and Synthesis-Dependent Luminescence Properties of Individual Single-Walled Carbon Nanotubes. *ACS Nano* **2009**, *3*, 2153−2156.

(18) Cognet, L.; Tsyboulski, D. A.; Rocha, J.-D. R.; Doyle, C. D.; Tour, J. M.; Weisman, R. B. Stepwise Quenching of Exciton Fluorescence in Carbon Nanotubes by Single-Molecule Reactions. *Science* **2007**, *316*, 1465−1468.

(19) Hertel, T.; Himmelein, S.; Ackermann, T.; Stich, D.; Crochet, J. Diffusion Limited Photoluminescence Quantum Yields in 1-D Semiconductors: Single-Wall Carbon Nanotubes. *ACS Nano* **2010**, *4*, 7161−7168.

(20) Crochet, J. J.; Duque, J. G.; Werner, J. H.; Doorn, S. K. Photoluminescence Imaging of Electronic-Impurity-Induced Exciton Quenching In Single-Walled Carbon Nanotubes. *Nat. Nanotechnol.* **2012**, *7*, 126−132.

(21) Gao, Z.; Danné, N.; Godin, A. G.; Lounis, B.; Cognet, L. Evaluation of Different Single-Walled Carbon Nanotube Surface Coatings for Single-Particle Tracking Applications in Biological Environments. *Nanomaterials* **2017**, *7*, 393.

(22) Hong, G.; Diao, S.; Antaris, A. L.; Dai, H. Carbon Nanomaterials for Biological Imaging and Nanomedicinal Therapy. *Chem. Rev.* **2015**, *115*, 10816−10906.

(23) Gao, Z.; Varela, J. A.; Groc, L.; Lounis, B.; Cognet, L. Toward the Suppression of Cellular Toxicity From Single-Walled Carbon Nanotubes. *Biomater. Sci.* **2016**, *4*, 230−244.

(24) Ghosh, S.; Bachilo, S. M.; Weisman, R. B. Advanced Sorting of Single-Walled Carbon nanotubes by Nonlinear Density-Gradient ultracentrifugation. *Nat. Nanotechnol.* **2010**, *5*, 443−450.

(25) Jacques, S. L. Optical Properties of Biological Tissues: a Review. *Phys. Med. Biol.* **2013**, *58*, R37−R61.

(26) McIlwain, H.; Bachelard, H. S. *Biochemistry and the Central Nervous System*, 5th ed.; Churchill Livingstone: Edinburgh, 1985.

(27) O'Brien, J. S.; Sampson, E. L. Lipid Composition of the Normal Human Brain: Gray Matter, White Matter, and Myelin. *J. Lipid Res.* **1965**, *6*, 537−544.

(28) Ghosh, S.; Bachilo, S. M.; Simonette, R. A.; Beckingham, K. M.; Weisman, R. B. Oxygen Doping Modifies Near-Infrared Band Gaps in Fluorescent Single-Walled Carbon Nanotubes. *Science* **2010**, *330*, 1656−1659.

(29) Varela, J. A.; Dupuis, J. P.; Etchepare, L.; Espana, A. E. S.; Cognet, L.; Groc, L. Targeting Neurotransmitter Receptors with Nanoparticles in Vivo Allows Single-Molecule Tracking in Acute Brain Slices. *Nat. Commun.* **2016**, *7*, 10947.

(30) Cooper, T. E.; Trezek, G. J. Correlation of Thermal Properties of Some Human Tissue with Water Content. *Aerospace Med.* **1971**, *42*, 24−27.

(31) Kim, M.; Adamska, L.; Hartmann, N. F.; Kwon, H.; Liu, J.; Velizhanin, K. A.; Piao, Y.; Powell, L. R.; Meany, B.; Doorn, S. K.; Tretiak, S.; Wang, Y. Fluorescent Carbon Nanotube Defects Manifest Substantial Vibrational Reorganization. *J. Phys. Chem. C* **2016**, *120*, 11268−11276.

■ NOTE ADDED AFTER ASAP PUBLICATION

This paper was originally published ASAP on December 8, 2017. Due to a production error, there was an error in Table 1. The corrected version was reposted on December 11, 2017.